Photonic-Crystal-Resonator Based Corner Reflector With Angle-of-Arrival Sensing

SUBMISSION DATE / POSTED DATE

26-05-2023 / 30-05-2023

CITATION

Alhaj Abbas, Ali; Zhao, Yixiong; Balzer, Jan; Solbach, Klaus; Kaiser, Thomas (2023). Photonic-Crystal-Resonator Based Corner Reflector With Angle-of-Arrival Sensing. TechRxiv. Preprint. https://doi.org/10.36227/techrxiv.23216498.v1

DOI

10.36227/techrxiv.23216498.v1

Photonic-Crystal-Resonator Based Corner Reflector With Angle-of-Arrival Sensing

Ali Alhaj Abbas , Yixiong Zhao , Jan Balzer, Klaus Solbach and Thomas Kaiser

***Abstract*—In this paper, we propose a Photonic Crystal (PhC) resonator based corner reflector for sensing the Angle-of-Arrival (AoA) of the incident wave from an interrogator. The sensor is constructed of joining a flat metal plate with a one-dimensional PhC resonator at an angle of 90°. The PhC resonator is designed by inserting a defect layer between two quarter-wave Bragg mirrors in order to create a deep notch in the backscattering. While the PhC resonator provides unique spectral signatures in the "specular direction" related to AoA (i.e. by shifting the notch position), the corner configuration allows the back-scattering of these signatures to the direction of the interrogator. As a proof of concept, EM simulation and measurement are performed in W-band on a 40-mm squared PhC resonator perpendicularly joined with a same size metal plate. Based on signatures, a resolution of less than 6° can be achieved in the angular range -35° to 35°. Due to the corner configuration that allows a high Radar Cross Section (RCS), the proposed sensor shows the potential of sensing the AoA at long reading ranges.**

***Index Terms*—Angle-of-Arrival sensing, one-dimensional photonic crystal resonator, corner reflector, Radar Cross Section (RCS).**

I. Introduction

The concept of wireless identification by means of electromagnetic radio frequency (i.e. RFID technology) became the foundation stone of a new paradigm shift in a multitude of applications that allow a high degree of automation. RFID technology is also considered as one of the enabling technologies for a world of addressable intelligence run by the Internet of things (IoT) [1], [2]. For RFID systems that consider lowering the infrastructure cost as the main concern, chipless RFID tags that employ no chip in their structure is considered the ultimate solution [3]. However, the absence of chips creates many challenges still being addressed by generous research including the coding capacity [4], reading range [5], [6], retro-directivity [7], [8] and detection reliability in harsh environments [9], [10].

Currently, the research zone of RFID tags has been enlarged from "item identification" to include other functionalities, like sensing [11]. Many research efforts contribute in this direction by establishing a different type of sensors, like structural (e.g. [12]) and environmental sensors (e.g. [13]). In fact, Angle-of-Arrival (AoA) is an attractive sensing parameter in RFID-based localization systems [14]–[16] which can be used as essential or supplementary knowledge of a reader to increase the localization accuracy. In conventional systems, the tag scattered signals are received by a sensor array at the reader side in order to estimate AoA which requires immense hardware implementation and advanced algorithms for high resolution [17]–[19]. In comparison, AoA sensors relocate the problem of angle sensing from the reader side to the tag side by coding different angles by different backscattered spectra which are readily measurable by a single antenna reader [20]. In the literature, we found a limited number of reported AoA or rotation sensors which were originally designed to detect the rotation of RFID tags attached to items. In [21], authors show the rotation sensing capability of a split-ring resonator tag utilizing the tag polarization diversity, but with low performance of 20° resolution. The proposed sensor in [22] and its improved version in [23] used another method of sensing based on collecting cross-polar responses of a set of dipoles. Although the sensor has shown a better angle resolution, the design suffered from angle ambiguity due to the lack of univocal cross-polar response related to a unique angle. Better performance has been demonstrated in [24], [25] using similar designs based on analytical expressions that relate the co- [24] or cross-polarization [25] response with the angle of rotation. Finally, in [20], the most relevant reference to our current work from an application perspective, Abbas *et.al* combined different-size dielectric resonators with a spherical lens in order to sense the incidence angle making the design advisable as anchors in RFID-based localization systems.

All existing AoA sensors were devised in the microwave frequency range where dimensions are easily realizable. Nevertheless, realizing such designs at mm-wave (30 to 330 GHz) or terahertz frequencies (100 GHz to 10 THz) requires scaling down the sensor dimensions to sub-mm range causing difficulty in fabrication [20]. Furthermore, at microwave frequencies the maximum achieved reading range is limited to tens of cm's because of the small aperture size of resonator structures, e.g. maximum range of 20 cm in [23] and up to 40 cm in [24], [25]. For operation at higher frequencies, the RCS level is also lowered by a square of wavelength which reduces the range more and complicates the detection of backscattered signatures. Indeed, mm-wave or terahertz frequency band offers additional benefits over microwave range in terms of bandwidth, resolution, and security [26]. Consequently, new tag classes have been recently built in such bands, based on dielectric resonators [27], [28], one-dimensional [29] and

Manuscript received May 26, 2021. This work was supported by the Deutsche Forschungsgemeinschaft (DFG, German Research Foundation) - Project- ID 287022738 - TRR 196, project S04, S01, and M05. (*Corresponding author: Ali Alhaj Abbas*).

A. Alhaj Abbas, K. Solbach and T. Kaiser are with Institute of Digital Signal Processing, University of Duisburg-Essen, Duisburg, Germany (e-mail: ali.alhaj-abbas@uni-due.de; klaus.solbach@uni-due.de; thomas.kaiser@uni-due.de).

Y. Zhao, J. Balzer are with Chair of Communication Systems (NTS), Faculty of Engineering, University of Duisburg-Essen (UDE), 47057 Duisburg, Germany (e-mail: yixiong.zhao@uni-due.de; jan.balzer@uni-due.de).

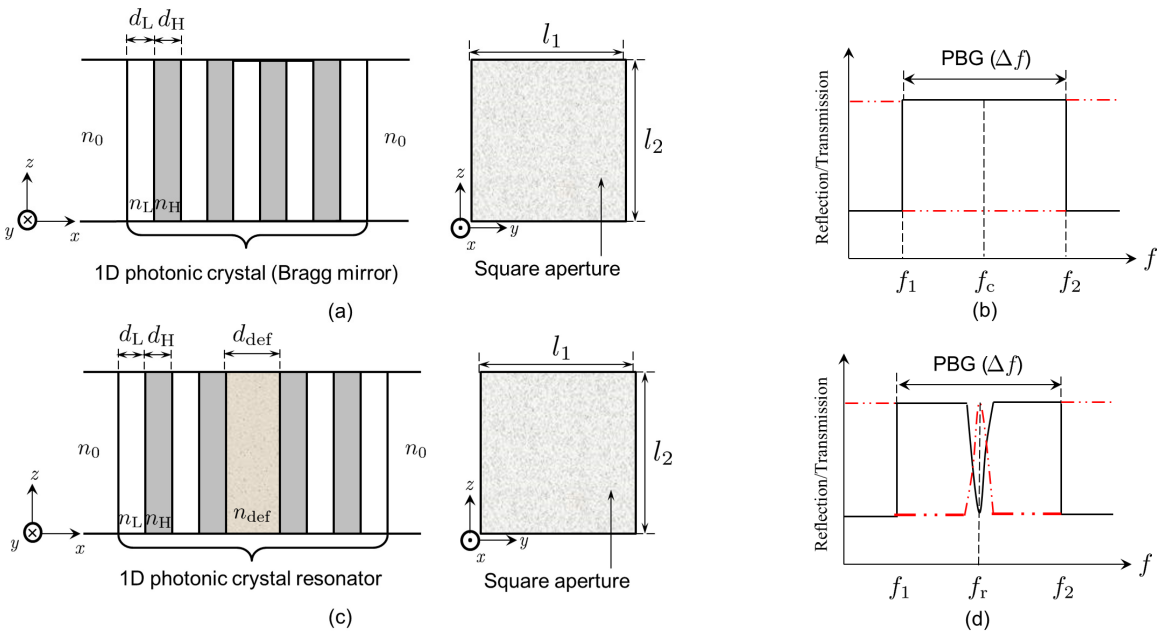

Fig. 1. (a) 1D PhC (Bragg mirror) having a periodicity along x-direction and a square aperture ($l_1 = l_2$) in yz-plane, (b) illustration of PBG principle mode behaviour, (c) schematic of 1D PhC resonator created by adding a defect layer, and (d) illustration of defect mode principle. The solid line represents the reflection, and the dashed line represents the transmission

two-dimensional Photonic Crystal (PhC) resonators [30], [31]. The most attractive class amongst them is PhC resonators due to ease of realization from low-loss materials [32]. In principle, PhC resonators are designed by placing a defect layer in a crystal lattice of two materials alternating in the refractive index (necessarily with sufficient contrast of low and high indices) to break the lattice periodicity and produce a resonance within the Photonic Band Gap (PBG) [33]. The defect mode frequency can be tuned by varying the angle of incidence where a shift toward higher resonance frequencies occurs by increasing the angle [34]. This interesting feature has been exploited in many applications in the optical range like building spatial filters [35].

In this paper, we propose a novel design of a mm-wave AoA sensor mainly suitable, but not limited to, for RFID-based localization systems operating in the W-band (75-110) GHz. The sensor is made of uniting a metal plate with a one-dimensional PhC resonator, joined to form a 90° corner. The basic idea is to use a PhC resonator to create distinct spectral signatures related to AoA and reflect these signatures in the specular direction. Then, thanks to the corner reflector, all spectral signatures are reflected back to the interrogator direction allowing for a high RCS level (corresponding to a long reading range) over a wide-angle, yet with a wide dynamic range of angular sensing.

It is worth mentioning that the corner reflector with its original design comprising two conducting surfaces has been widely used as an efficient reflector with a high RCS to increase target visibility where no information has been encoded in the structure [36]. Just recently, we witness smart corner reflectors with identification capabilities coded in amplitude as in [37] and in frequency by dielectric resonators [6], [28], [38] and by frequency selective surface (FSS) [39]. Contrary to designs of coded reflectors for discrimination and identification, our present paper demonstrates an new functionality of AoA sensing.

The rest of this paper is structured as follows: first, the design details and the analysis of the angle-dependent scattering of a PhC resonator are presented in Section II. In Section III, we provide a detailed description of the AoA sensor supported by EM simulation results. Section IV presents the fabrication of the sensor and experimental results endorsing EM simulations. In this section, we also discuss the sensor performance based on measured results. Finally, we conclude the paper in section V.

II. One-dimensional Photonic Crystal Resonators

Photonic crystals (PhCs) are periodic structures made of dielectric materials that own a periodic function of refractive indices [33]. Owing to the periodicity and the sufficient contrast of the dielectric constant of the crystal lattice, an artificial phenomenon that does not exist in natural materials, like the Photonic Band Gap (PBG), can be produced. PBG is the property of prohibiting mode propagation at a specific range of frequencies. In principle, the PBG is created by the destructive interference of the multiple reflected waves at material interfaces with the forward-propagating waves. Due to the periodicity, elimination of forward propagation is caused, i.e., a complete reflection. The periodicity can be engineered to produce a PBG in one (1D), two (2D), or three-dimensions (3D). A 1D PhC or the so-called Bragg mirror is built of a stack of multilayers that alternate between low- and high-refractive indices (n_L and n_H respectively) whose thicknesses are d_L and d_H, respectively, see Fig.1(a) for a 1D PhC with a square aperture and a periodicity designed in the x-direction. Fig.1(b) shows an illustration of the PBG principle

which is caused by exciting a Bragg mirror of large aperture dimensions (i.e. compared to the wavelength) using a plane wave propagated in the -x-direction. The figure clarifies the high level of reflectance compared to the low transmission level in the PBG. The PBG center frequency (f_c) and its bandedges (f_1 and f_2) are calculated as follows [40]:

$$f_c = \frac{c}{2(n_L d_L + n_H d_H)} \tag{1}$$

$$f_1 = c\frac{\cos^{-1}(\rho)}{\pi(n_L d_L + n_H d_H)} \tag{2}$$

$$f_2 = c\frac{\cos^{-1}(-\rho)}{\pi(n_L d_L + n_H d_H)} \tag{3}$$

where c is the speed of light and $\rho = (n_H - n_L)/(n_H + n_L)$ representing the Fresnel reflection coefficient at the low-high interface. From the bandedge frequencies, we can calculate the bandwidth of the PBG (Δf) as follows:

$$\Delta f = \frac{2c}{\pi}\frac{\sin^{-1}(\rho)}{n_L d_L + n_H d_H} \tag{4}$$

From these equations, we conclude that the higher is the contrast between the refractive indices, the wider is the bandwidth of the PBG. Furthermore, we can maximize the reflection within the PBG bandwidth by choosing the optical thickness of layers a quarter-wavelength of the band gap center frequency ($n_L d_L = n_H d_H = \lambda_c/4$) and increasing the number of layers. Therefore, with high material contrast and a sufficiently large number of layers, we can design an efficient all-dielectric reflector over a wide bandwidth.

If the periodicity of a Bragg mirror is broken by a defect layer as shown in Fig.1(c), the structure generates a narrow resonance in the PBG: a notch in the reflection mode and a peak in the transmission mode, see Fig.1(d). The position and the quality factor of the defect mode can be altered by mainly controlling the thickness or the refractive index of the defect layer. The higher is the refractive index and the higher is the thickness of the defect layer, the lower is the frequency of the defect mode. However, further increasing of the refractive index or the thickness causes the occurrence of multiple modes within the PBG after reaching a certain level [41], [42]. If we even vary the location of the defect mode in the lattice, the defect mode will still be excited, but, with a lower peak level in the transmission [43]. Considering all these factors and with the help of equations (1)-(4), we design a Bragg mirror in the W-band to provide a PBG in the frequency range $f_1 \approx 69$ GHz to $f_2 \approx 116$ GHz ($f_c \approx 92.5$ GHz) by using two materials with a sufficient contrast in the refractive index: $n_L = \sqrt{2}$ and $n_H = \sqrt{10.2}$. The thicknesses of the low-index and high-index layers are selected a quarter-wavelength of the PBG center frequency: $d_L = 0.57$ mm and $d_H = 0.254$ mm, respectively.

On the other hand, we design a PhC resonator by introducing a defect layer at the center between two Bragg mirrors of 4 layers, see Fig.1(c). Ignoring the phase delay produced by the mirror, the frequency of the first-order (half-wavelength) cavity mode (f_d) is related to the defect layer dimensions as follows:

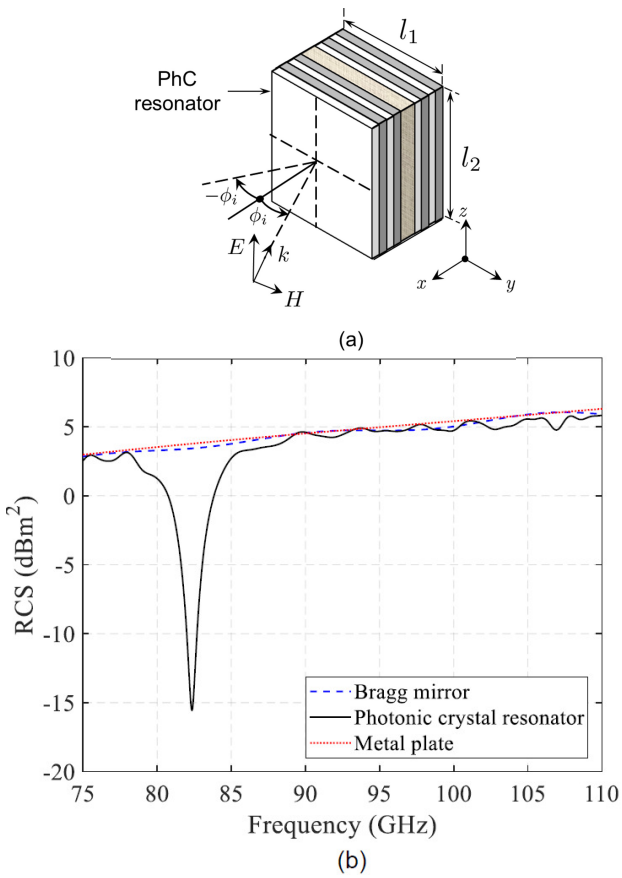

Fig. 2. (a) EM excitation of a PhC resonator by TE polarized plane wave at $\phi_i = 0$ and (b) mono-static RCS of a PhC resonator compared to the mono-static RCS of a Bragg mirror and of a metallic plate (40 mm × 40 mm). Bragg mirror and PhC resonator common parameters are $l_1 = l_2 = 40$ mm, $n_L = \sqrt{2}$, $n_H = \sqrt{10.2}$, $d_L = 0.254$ mm, $d_H = 0.57$ mm. Defect layer parameters are $d_{def} = 1.37$ mm, $n_{def} = \sqrt{2}$.

$$f_d = \frac{c}{2n_{def}\ d_{def}} \tag{5}$$

However, it has been proven that the resonance frequency is also greatly affected by band gap center frequency and mirror penetration depth [44]–[46]; estimated formulas can be found in [44]. For our design, we fix the refractive index of the defect layer to $n_{def} = \sqrt{2.0}$ and then using the Transfer Matrix Method (TMM), e.g. [47], we find that a defect layer thickness of 1.37 mm produces a resonance frequency at 82.8 GHz.

Fig.2(a) shows the excitation of a PhC resonator by a TE polarized plane wave where the electric field is directed to the z-axis under an angle of incidence (ϕ_i). In Fig.2(b), we plot the simulated mono-static scattering cross section (RCS) of the designed Bragg mirror and resonator under normal incidence excitation ($\phi_i = 0$); the simulations are performed using the transient solver of CST Microwave Studio. Both designs have a finite, but electrically large, aperture of $l_1 = l_2 = 40$ mm, $\approx 12\lambda_c$ (the wavelength of PGB center). As expected, the Bragg mirror scatters like a metallic plate of the same dimensions where cross section of scattering can be estimated using formula (6) [48]:

$$RCS_{\text{plate}}(f) = \frac{4\pi(l_1 l_2)^2 f^2}{c^2} \tag{6}$$

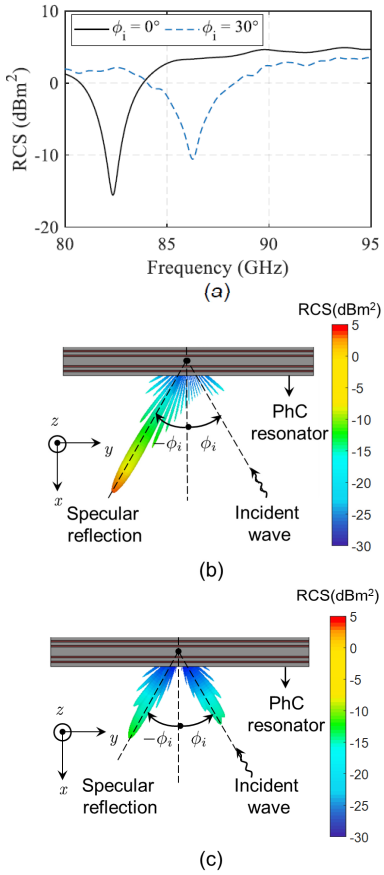

Fig. 3. (a) Simulated mono-static RCS of PhC resonator excited normally and simulated bi-static RCS for oblique excitation at $\phi_i = 30°$, and Bi-static RCS (dBm^2) of PhC resonator for $\phi_i = 30°$ (b) outside notch frequency at 92.5 GHz and (c) at notch frequency of 86.27 GHz. Bi-static RCS patterns are plotted in the range ($-90° \leq \phi \leq 90°$)

where l_1 and l_2 are respectively the length and the width of the plate. In comparison, the PhC resonator produces a deep notch at 82.35 GHz in the PBG with a small deviation from the value obtained by TMM. The notch 3 dB-bandwidth is 3.2 GHz which makes a quality factor of 25. Outside the notch, we see a high level of scattering close to the case of a Bragg mirror.

If we interrogate the resonator at an angle different from the normal incidence angle (i.e. $\phi_\mathrm{i} \neq 0$), the Snell's law applies and the resonator reflects the incoming wave effectively to the specular direction ($\phi_\mathrm{r} = -\phi_\mathrm{i}$). Additionally, the resonator produces an angular-dependent shift in the specular reflections represented by a shift in the notch position. This behavior is caused by the reduction in the equivalent optical thickness from $n_\mathrm{def}\ d_\mathrm{def}$ in the case of normal incidence to $n_\mathrm{def}\ d_\mathrm{def}$ $\cos(\phi_\mathrm{def})$ for the case of oblique incidence; ϕ_def is the angle of transmission in the defect layer. Therefore, the resonator is equivalently thinner for higher angle of incidence which corresponds to an increase in the resonance frequency within the PBG. As an example, Fig.3(a) shows the mono-static RCS of a PhC resonator excited by oblique incidence under $\phi_i = 30°$. As expected, compared to the normal incidence case we observe a shift in the resonance frequency with a decrease in the notch depth besides some variations outside the notch.

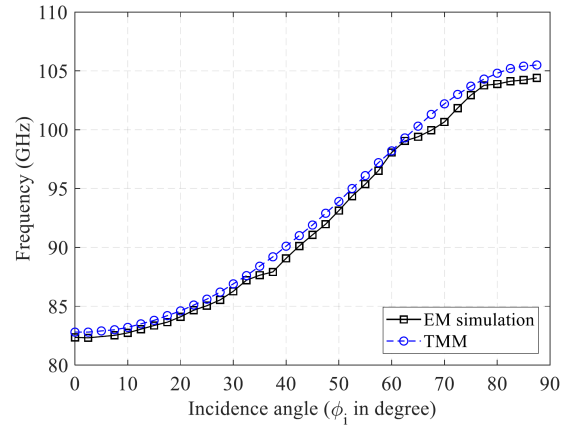

Fig. 4. Notch frequency position as a function of incidence angle using EM simulations and TMM

It is also interesting to see the bi-static RCS of the PhC resonator as the angle of incidence deviated from the normal. Here, we focus on the relevant scattering in our subsequent investigation, the retro-scattering and the specular scattering, and disregard the discussion on the transmitted wave. We choose $\phi_i = 30°$ to clarify this scattering behavior and then we generalize the concept to all different angles. As can be seen in Fig.3(b), the bi-static RCS outside the notch frequency ($f = 92.5$ GHz) exhibits a strong reflection in the specular direction with very low contributions in the retro-direction. This is because outside the resonance the structure acts as an efficient reflector and for sufficiently large dimensions Snell's law is satisfied. At the notch frequency as indicated in Fig.3(c), we also see a low reflection in the specular direction whose amplitude is in agreement with the notch depth shown in Fig.3(a). Therefore, the PhC resonator does not only create a useful behavior of modulating spectral signatures as a function of angle, but it also reflects these signatures effectively in the specular reflection. The design of our proposed AoA sensor is mainly revolved around these behaviors as will be clarified in the next section.

For all angles ranging from 0° to less than 90°, we extracted the spectral signatures in the specular reflection using EM simulation and then measured the notch frequency. The results are plotted in Fig.4 supported by TMM where we observe a satisfactory agreement. The resonance frequency position is proportional to the the propagation angle ϕ_def in the defect layer by cos (ϕ_def) which is related to the incidence angle by Snell's law, equation (7):

$$\cos(\phi_\mathrm{def}) = \sqrt{1 - \frac{n_0}{n_\mathrm{def}} \sin^2(\phi_\mathrm{i})} \tag{7}$$

More specifically, the equivalent optical thickness of the defect layer reduces as we increase the angle of incidence which justifies the increase in the resonance frequency. However, the increase behaves differently over the entire range: for low angles of incidence, the frequency increases slightly with a shallow slope. Further increase in the angle establishes a steeper slope which means that we obtain a greater change in frequency for a given change in angle. For a high angle

of incidence, the curve shallows out again where we observe a small change in frequency in response to a change in angle. This relation has a great influence on determining the angular sensing resolution and range as will be clarified in the following sections.

III. AoA sensing using PhC Resonator Based Corner Reflector

Corner reflectors are widely used as high RCS retro-directive targets or as calibration targets in many radar applications [49]. The simplest geometry of corner reflectors, i.e. the so-called dihedral, employs two conducting plates joined together at 90° angle forming a "corner". When a corner reflector is excited by an electromagnetic wave, the specular reflection caused by one plate hits the other plate which, in turn, reflects it back to the direction of the interrogator. In this sense, corner reflectors are mainly characterized by a broadband response over a wide-angle of incidence [36]. For our design, we utilize the same principle of corner reflector but instead of using two metal plates that contain no information in the backscattering, we join a PhC resonator with a metal plate as illustrated in Fig.5. The incident wave of our interest has a TE polarization (the electric field is directed to the z-axis) with a propagation direction denoted by k vector. We assume that the incident wave makes an angle ($-45° \leq \phi_i \leq 45°$) with the corner reflector axis of symmetry. As also illustrated, the incoming waves hit the PhC resonator by an angle (ϕ_{i1}) then bounces off to the metal plate by an angle (ϕ_{i2}) where $\phi_{i1} = \phi_i + 45°$ and $\phi_{i2} = -\phi_i + 45°$. It is important to point out that the angles illustrated in Fig.4 are equivalent to the angles ϕ_{i1} that we will use in this section.

To demonstrate the working principle of the sensor, we have used the designed PhC resonator in the previous section. The PhC resonator is combined with a square metal plate with the same dimensions of $l_1 = l_2 = 40$ mm. When the whole geometry is excited under an angle $\phi_i = 0°$, the incident waves

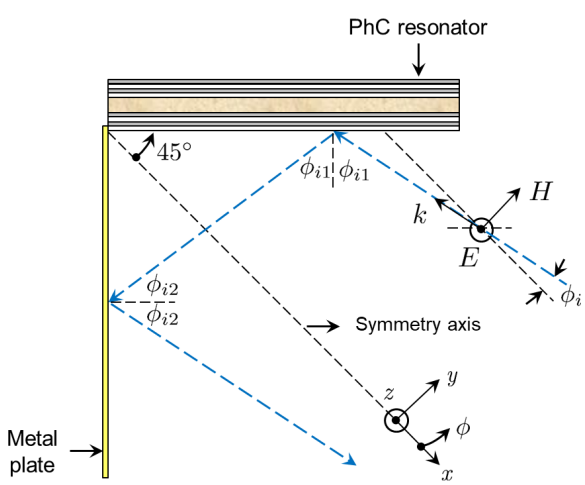

Fig. 5. Geometrical model of the proposed AoA sensor showing the incident and reflected rays with their representative angles (edge view). ϕ_i is the angle of incidence taken from the axis of symmetry of the corner reflector while ϕ_{i1} and ϕ_{i2} represent the incidence or reflected angle of rays related to PhC resonator and metal plate, respectively

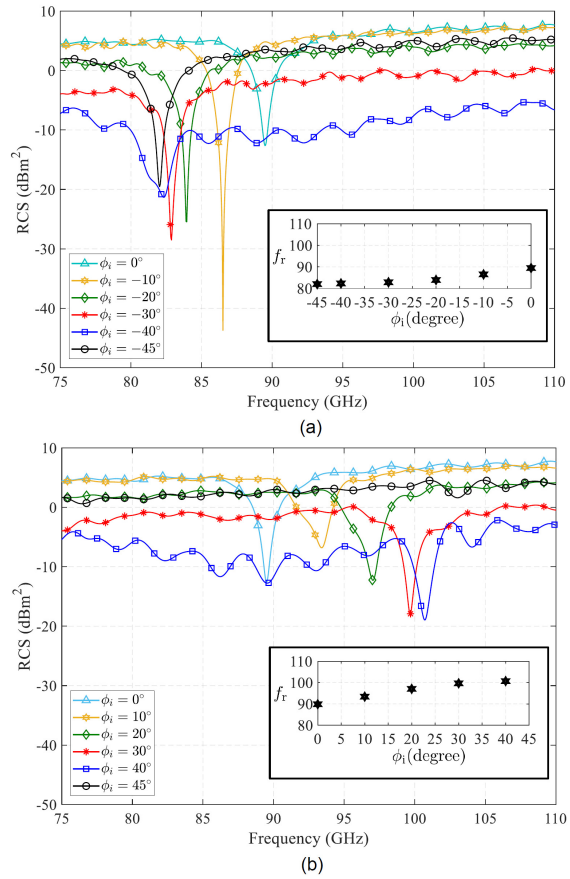

Fig. 6. Simulated mono-static RCS of AoA sensor (a) for some negative incident angles between $-45°$ and $0°$ and (b) for some positive incident angles between $0°$ and $45°$. Inset – notch frequency position as a function of angle of incidence.

impinge on the PhC resonator at an angle $\phi_{i1} = 45°$. As a result of two specular reflections, the backscattered signal in the mono-static direction carries a notch at about 90 GHz which is very close to the frequency observed in the specular reflection when the PhC resonator is excited alone, see Fig.6 at $\phi_i = 0°$ and Fig.4 at $45°$ for comparison. Furthermore, a high RCS of 5 dBm^2 is produced outside the notch due to double-bounce reflections and low spill-over losses from the plate edges. Moving to $\phi_i = -10°$, we recognize a shift in the resonance frequency to about 86.5 GHz because of the angle-dependent scattering behavior of the PhC resonator interpreted earlier. A little variation in the RCS outside the notch is observed for this angle compared to the boresight angle. An additional decrease in the notch position of about 2.6 GHz is examined for a further ten-degree deviation in the angle, $\phi_i = -20°$. Nevertheless, if we increase the angle beyond this limit, we notice a smaller variation in the notch position for even a substantial change in the angle; an angle deviation from $-30°$ to $-45°$ causes around 0.7 GHz down-shift in the frequency. Further, the RCS is degraded as we increase the angle to reach a minimum at $-40°$ due to losses made by the corner edge diffraction. Specifically at this angle, the notch is partially obscured by the rippled response which can make successful notch detection susceptible to any additional noise. At angle $\phi_i = -45°$ coinciding with the PhC resonator, the

PhC resonator mostly contributes to the backscattered wave with a minimal effect from the metal plate. Hence, as can be seen in Fig.6(a), the RCS exhibits a notch frequency at about 82.03 GHz which is very close to the normal incidence case of a PhC resonator alone. At this angle, the RCS returns to high level outside the notch compared to $\phi_i = 40°$.

For positive angles of incidence ($0° \leq \phi_i \leq 45°$), the EM waves strike the PhC resonator by angles in the range ($45 \leq \phi_{i1} \leq 90°$) which causes a shift in the notch position to higher frequencies as we increase the angle, see Fig.6(b). This is analogous to exciting the PhC resonator alone and following the notch shift in the specular direction, see Fig.4. For angles $0° \leq \phi_i \leq 30°$, a notable change in the frequency is obtained for a corresponding change in the angle of incidence. On the other hand, for larger angles the notch frequency position starts to converge and provide the least change in frequency. At $\phi_i = 45°$, the backscattered wave is dominated by the metal plate where we see a flat response without a notch.

The various frequency signatures can be analyzed by the reader based on measuring the notch position to correctly estimate the AoA. From the previous discussion, we conclude that the main two factors that affect the sensor performance are:

1) The produced frequency deviation (Δf) for a given change in the incidence angle ($\Delta\phi$) which is desirable to be as large as possible for easier discrimination between two adjacent angles.
2) The level of RCS, for a given angle of incidence, in which the notch is not distorted and can still be detected by the reader. Spectral signatures that provide high RCS outside the notch with a low influence on the notch shape and depth are desirable.

For high positive and negative angles of incidence off-boresight, we see that the sensor does not respond to a further change in the angle of incidence in terms of frequency shift, and also the RCS is reduced because of the growing effect of diffraction at edges. Therefore, the best performance is expected for angles around boresight in the range $[-\phi_i^{(\text{start})}, +\phi_i^{(\text{stop})}]$ which is determined by the factors mentioned earlier. We will discuss this in more detail in the next section based on experimental results.

IV. Fabrication and Experimental Verification

To realize the PhC resonator, we first fabricated several layers of two different materials of low and high indices. The low-index material layers were manufactured from Cyclic Olefin Copolymer (COC) ($\epsilon_r = 2$) using 3D printing, see Fig.7(a) (right). From this material, we realized several layers of 0.57 mm thickness to construct a Bragg mirror and one defect layer of 1.37 mm thickness for the cavity. For the high index material, we used the dielectric substrate produced by Rogers Corporation which is made of PTFE ceramic (RT/duroid 6010.2LM) and has a relative permittivity of 10.2, low tangent loss of 0.0013, and a thickness of 0.254 mm [50]. After the copper was removed from the dielectric material by etching, we cut 4 cm square pieces as shown in Fig.7(a) (left). The layers were manually assembled to produce the structure $(\text{LH})^2\text{D}(\text{HL})^2$, Fig.1(c), where a defect layer is inserted between two Bragg mirrors of 4 layers. The layers were fixed together by using a 58 μm thick transparent tape placed around the structure four edges as depicted in Fig.7(b). The AoA sensor was built by linking a metal plate attached to FR-4 substrate with the produced PhC resonator using a 30 μm double-sided adhesive, see Fig.8(a).

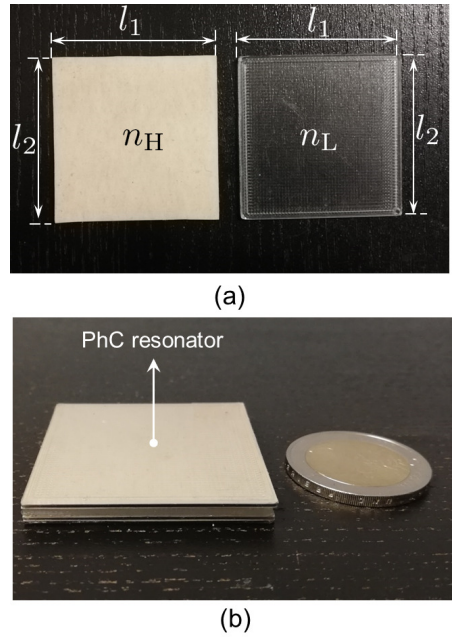

Fig. 7. (a) Two fabricated layers: (left) RT/duroid®6010.2LM ($n_{\text{H}} = \sqrt{10.2}$) and (right) COC material ($n_{\text{L}} = \sqrt{2.0}$) and (b) PhC resonator constructed of a stack of layers ($(\text{LH})^2\text{D}(\text{HL})^2$). L, H, and D denotes high index material, low index material, and defect layer, respectively. l_1 = l_2 = 4 cm

All measurements have been performed at W-band in an anechoic chamber using the R&S ZVA 67 Vector Network Analyzer (VNA) connected to a W-band extender (ZC110). The measurements were implemented in the whole range (75-110) GHz with 2001 frequency points. To reduce the noise level and improve the dynamic range, we used a 10 kHz IF filter bandwidth and an averaging operation over 10 samples per frequency point. A one-port (short) calibration has been also executed on the standard WR-10 waveguide of the extender before installing a 25 dBi horn antenna at the waveguide flange.

All Devices Under Test (DUT) were placed above a styrofoam slab fixed on a computer-controlled turntable (allowing for rotation in the azimuth plane) at a distance (d) in front of the horn aperture and positioned axially with the horn, see Fig.8(b). Due to the large reflection induced by the antenna mismatch, we used background subtraction in which the scattering parameter S_{11} is first measured without the DUT in place corresponding to "empty room" (S_{11}^{empty}) and then we subtracted the results from the measured S_{11} parameter with the DUT in place (S_{11}^{DUT}) [6], [51], [52]. The scattering signatures (mono-static RCS) were calculated by normalizing the measured reflection after subtraction (S_{11}^{DUT} - S_{11}^{empty}) to the measured reflection of a reference target with known RCS (S_{11}^{ref} - S_{11}^{empty}) using the following equation [53]:

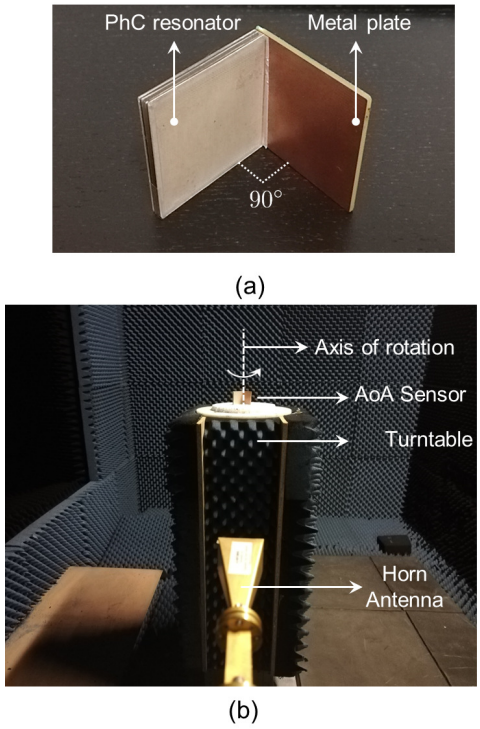

Fig. 8. (a) AoA sensor constructed of joining a 1D PhC with a metal plate attached to a layer of FR-4 substrate forming a corner shape and (b) experimental setup showing the AoA sensor positioned approximately 1m distance from a horn antenna (75 - 110) GHz

$$\sigma_{\text{DUT}} = \left| \frac{S_{11}^{\text{DUT}} - S_{11}^{\text{empty}}}{S_{11}^{\text{ref}} - S_{11}^{\text{empty}}} \right|^2 \cdot \sigma_{\text{ref}} \tag{8}$$

where σ_{DUT} and σ_{ref} are the RCS of the DUT and the reference target respectively. We chose a flat metallic plate of 4 cm $\times$ 4 cm size as a reference target with a known RCS which can be calculated using equation (6). After "empty room" subtraction, the residual noise produces a dynamic range of about 75 dB.

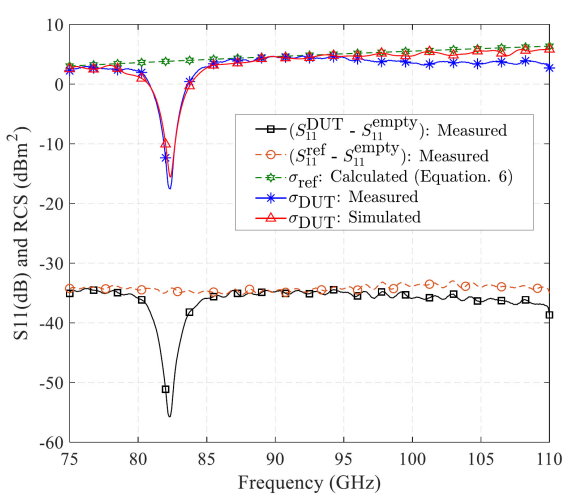

Fig. 9. Measured scattering parameter (S11) in dB and mono-static RCS in dBm^2 of a 1D PhC resonator (4 cm $\times$ 4 cm) for incidence at $\phi_i = 0°$ compared to the simulated results and the S11 and RCS of a metallic plate as a reference target used for RCS calculation for normal incidence

The first measurement was carried out by locating a PhC resonator alone at d $\approx$ 1m which fulfill the far-field conditions in the specified bandwidth. The measured mono-static RCS (σ_{DUT}) is plotted in Fig.9 with the simulated one. We also add to the figure the raw data used to obtain σ_{DUT} represented by the measured scattering parameters of the DUT and the reference target with its calculated RCS. The measured RCS is in very good agreement with the simulations where the cavity resonates at around 82.4 GHz and shows a high RCS outside the notch comparable to the RCS of a flat metallic plate of the same size.

A series of measurements have been then performed for the AoA sensor as a DUT allowing the turntable to rotate azimuthally to detect the spectral signatures as a function of angle. To avoid positioning error, an "empty room" calibration has been performed once at 0° incidence angle and used as a reference channel data for all other angles. This gave rise to an increase in the noise level for angles other than 0° from -75 dB to -60 dB. In Fig.10, we show the measured RCS for incidence angles of 0°, ±10°, ±20°, ±30°, ±40° and ±45°. The figure shows that each angle has a distinct spectral signature exemplified by the unique notch frequency position. Notches

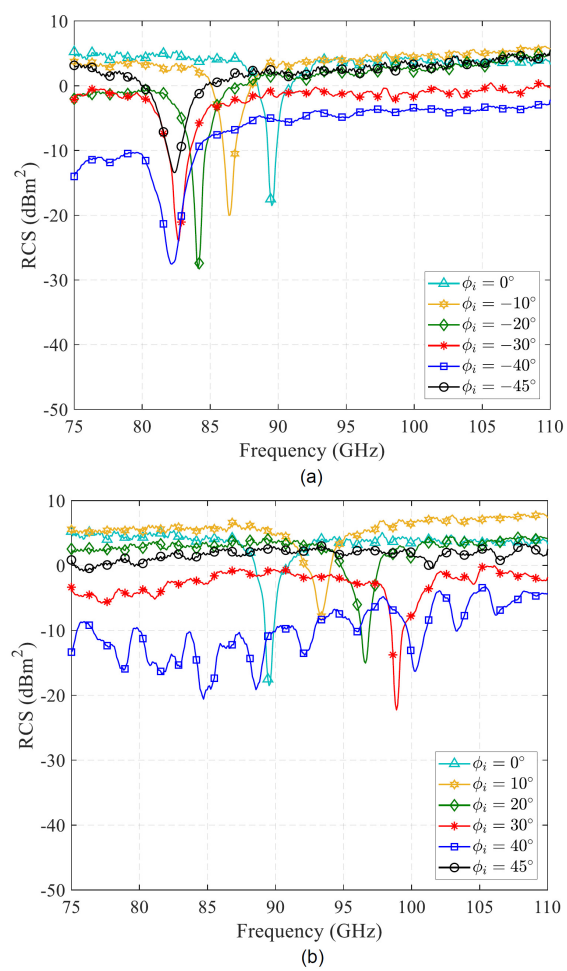

Fig. 10. Measured mono-static RCS of AoA sensor (a) for negative incident angles of $-45°$, $-40°$, $-30°$, $-20°$, and $-10°$, (b) for positive incident angles of 10°, 20°, 30°, 40° and 45°. Normal incidence case ($\phi_i = 0°$) is included in both subfigures for comparison

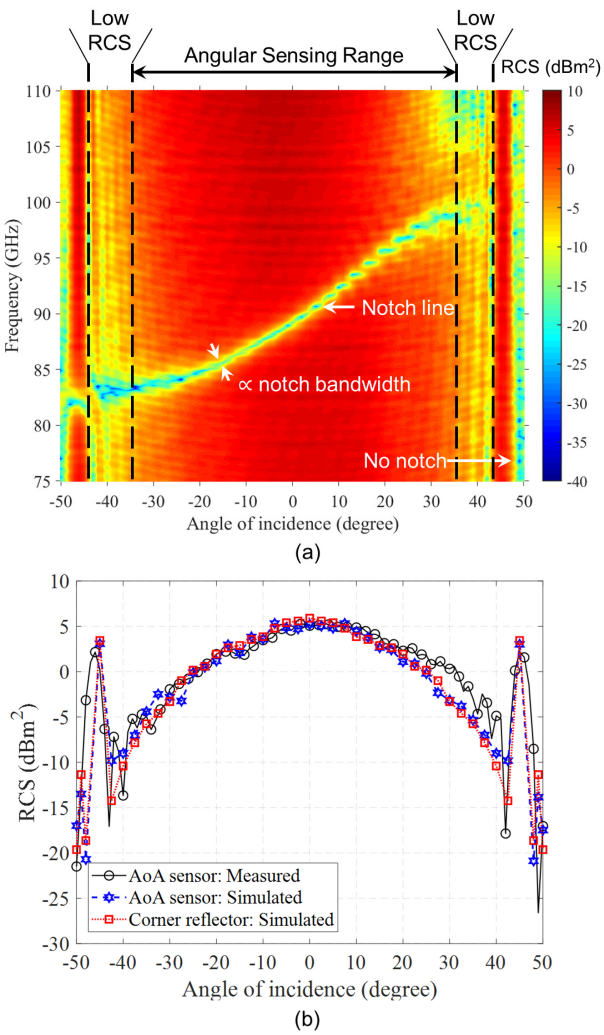

Fig. 11. (a) Measured mono-static RCS of AoA sensor over the range of incidence angles ϕ_i from $-50°$ to $50°$, (b) measured and simulated peak levels of monostatic RCS of AoA sensor outside the notch at $f = 78.5$ GHz compared to the simulated RCS peak levels of conventional corner reflector (4cm $\times$ 4cm)

.

are also differentiated by their bandwidth, shape, and depth. Compared to simulated results, we observe some discrepancies in the notch depth and position and some variation in the RCS level. These differences can be attributed to fabrication tolerances and errors from assembling and also to scattering effects of the environment which are not calibrated out by the empty room subtraction. In Fig.11(a), mono-static spectral signatures are plotted for angle of incidence from $-50°$ to $50°$ in small steps of $1°$. In the range from $-35°$ to $35°$, we see a notch line of low RCS values and with varying width where angles of incidence are uniquely related to notch positions or shapes. The intensity of the line represents the notch depth while the width of the line is proportional to the notch bandwidth. For negative angles, we see smoother transitions in the resonance frequencies along angles compared to some discontinuities at some positive angles since for positive angles we see an increased retro-directive scattering from the PhC resonator, see Fig.3, which is constructively or destructively superimposed with the scattering from the corner reflector causing a small splitting of notches at some angles and a convergence of notches to each other. For a greater angle of incidence, less than $-35°$ and greater than $35°$, the RCS starts to reduce dramatically causing a distortion of the notch and a difficultly in discrimination, see the zone of low RCS in Fig.11(a) where the notch is seen to be immersed in a rippled response. Fig.11(b) shows the RCS levels at $f = 78.5$ GHz (outside the notch line) as a function of angle of incidence which emphasize the high RCS around boresight and a poorer performance far from boresight, similar to the typical response of conventional dihedral corner reflectors.

The previous results of the AoA sensor have been taken at a distance $d \approx 0.87$ m. Fig.12 shows the variation of notch line (the angle of incidence versus the notch frequency) with the distance where the same set of measurements have been performed for two additional distances (1.14m and 1.6m). we observe very little variation in the notch position which emphasizes that the sensor is independent of the reading range.

Therefore, we examine the sensor performance in the angular sensing range $[-35, +35]$ where we obtain high RCS in the range -5 dBm$^2 \leq RCS \leq 5$ dBm^2. Without considering potential degradation effects of environmental clutter, this corresponds to maximum reading range varying from 12.5 m to 22.2 m, which is calculated using the Radar equation (9), assuming that the transmitted power $P_{\mathrm{T}} = 0$ dBm, the receiver sensitivity $P_{\mathrm{R}} = -80$ dBm, and the reader antenna gain $G_{\mathrm{T}} = 25$ dB [54], [55].

$$R_{\max} = \sqrt[4]{\frac{P_{\mathrm{T}} G^2 \lambda^2 \sigma}{(4\pi)^3 P_{\mathrm{R}}}} \tag{9}$$

The performance of the sensor depends on the detection and decoding processes at the reader side. Detection can be achieved by notch detection algorithms upon which the reader should be able to recover the notch and find its position [56], [57]. Then, in the decoding stage, the reader maps the notch position to its corresponding angle of incidence. Here,

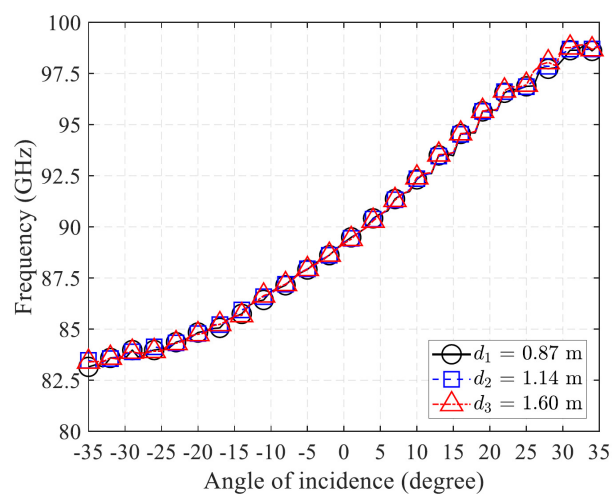

Fig. 12. Variation of notch line as a function of distance

.

we pre-assume that the notch is successfully detected by our measurement device under the prescribed conditions in noise and channel. Therefore, the subsequent discussion is only related to the decoding reliability based on measured spectral signatures where we define the angular resolution that can be reached. The angle resolution is directly related to the frequency resolution that can be achieved by the reader. We mean by frequency resolution the minimum frequency spacing between two notch positions that can be unambiguously distinguished by the reader. To parameterize these words, we define the frequency spacing $\Delta f(\phi_{\mathrm{k}}, \phi_{\mathrm{j}})$ as the difference between the notch frequency of angle ϕ_{k} with all other angles ϕ_{i} where $i = 1, 2, 3, ...71$ ($\phi_1 = -35°$ and $\phi_{71} = 35°$), as follows [23]:

$$\Delta f(\phi_{\mathrm{k}}, \phi_{\mathrm{j}}) = |f(\phi_{\mathrm{k}}) - f(\phi_{\mathrm{i}})| \tag{10}$$

where the notch frequency is measured for each angle as the minimum value in the signature.

Moreover, we relate the Δf parameter with three different reader frequency resolutions (f_{res} = 0, 0.2 GHz, and 0.4 GHz) through four conditions: (1) $\Delta f = 0$, (2) $0 < \Delta f \leq 0.2$, (3) $0.2 < \Delta f \leq 0.4$, and (4) $\Delta f \geq 0.4$. In Fig.13, we plot Δf where each pixel represents the frequency difference between measured notch positions of angle ϕ_{i} and ϕ_{j}. A frequency separation $\Delta f = 0$ should be obtained when $\phi_{\mathrm{i}} = \phi_{\mathrm{j}}$ represented by a diagonal line in Fig.13, however, we observe ambiguity at some angles like $-29°$ which has the same notch frequency as $-26°$. Scanning over all angles produces a maximum error in decoding of $3°$, an averaged error of $0.17°$. For case (2), we observe an increased ambiguity around the diagonal line with a maximum error of $5°$. Lowering the frequency resolution of the reader to the case (3) causes additional errors mainly to occur for high negative and positive angles with a maximum error of $6°$. This is expected behavior due to the convergence of notches at these angles. Less ambiguity can be achieved around boresight due to the sufficient frequency spacing between adjacent angles. Case (4) indicates that the reader can unambiguously decode the notch positions to their respective angles without errors. Accordingly, for a frequency resolution of 0.4 GHz, the reader can recover the angle of incidence from the signature with an average error of $1.65°$ over the complete interval.

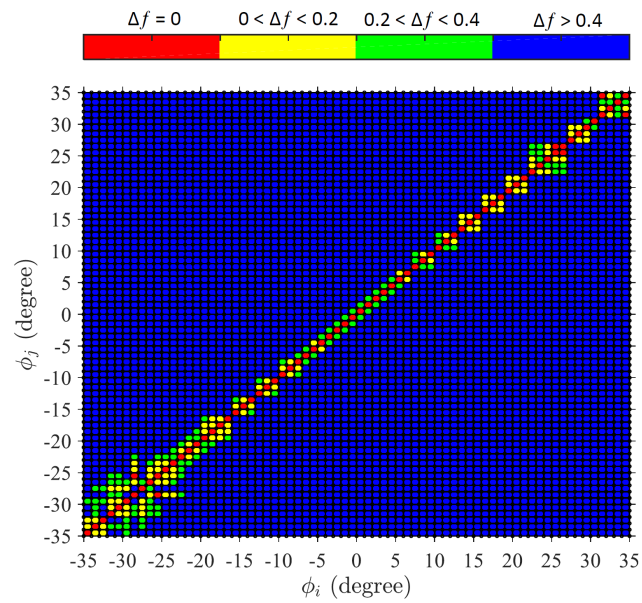

Fig. 13. Mapping of the frequency spacing parameter Δf as a function of ϕ_{i} and ϕ_{j} over a set of four quantized intervals. Angles take the values from $-35°$ to $35°$ with a fine resolution of $1°$.

V. Conclusion

In this paper, we presented a novel design of an AoA sensor based on combining a 1D PhC resonator with a metal plate under $90°$ angle. The sensor operation mainly relies on the angle-dependent scattering of the PhC resonator which produces notch signatures (position, shape, bandwidth) in its specular reflection which uniquely depend on the AoA of the interrogating RF wave. The corner geometry then steers all these signatures back to the reader's direction.

The sensor working principle was described by EM simulation and validated by experiment at millimeter-wave frequencies. Contrasted to other sensors in the literature, we demonstrated a large readout range of 1.6 m at this band due to the high RCS of backscattered signals, thanks to the corner reflector. The detection is performed by sweeping the whole frequency range searching for a notch in the spectrum. The notch position establishes "fingerprints" corresponding to certain reader signal incident angles. Considering a successful detection of the notch by the reader, we can realize an angular resolution less than $6°$ in the angular sensing range $[-35, +35]$ for a 0.4 GHz frequency resolution of the reader.

Higher angular resolution can be acquired by either improving the sensor design or developing advanced algorithms for detection. I.e., increasing the number of layers of the PhC resonator offers higher quality factor [44] aiding in reducing the overlapping between notches at adjacent angles and therefore enhancing the angular resolution. Algorithms that can detect not only the notch position but also the notch shape and bandwidth would improve the angular resolution as well [56], [57].

References

[1] R. Want, "An introduction to RFID technology," *IEEE Pervasive Computing*, vol. 5, no. 1, pp. 25-33, Jan.-March 2006.

[2] F. Zheng and T. Kaiser, "Digital Signal Processing for RFID, ser. Information and Communication Technology Series," Wiley, 2016.

[3] S. Preradovic and N. Karmakar, "Chipless RFID: Bar Code of the Future ", *IEEE Microwave Magazine*, vol. 11, pp. 87–97, Dec. 2010

[4] M. Khaliel, A. Fawky, A. El-Awamry, A. Mahmoud and T. Kaiser, "Printable, high coding capacity chipless RFID tags for low-cost item tagging," 2017 IEEE 14th International Conference on Networking, Sensing and Control (ICNSC), Calabria, 2017, pp. 351-355.

[5] A. Alhaj Abbas, M. El-Absi, A. Abuelhaija, K. Solbach and T. Kaiser, "RCS enhancement of dielectric resonator tag using spherical lens," *Frequenz*, vol.73, no.5–6, pp. 161–170, 2019.

[6] A. Alhaj Abbas, M. El-Absi, A. Abuelhaija, K. Solbach and T. Kaiser, "Corner Reflector with RCS Frequency Coding by Dielectric Resonators," *IET Microwaves, Antennas & Propagation*, vol. 15, no. 6, 2021.

[7] A. Alhaj Abbas, M. El-Absi, A. Abuelhaija, K. Solbach and T. Kaiser, "Wide-Angle RCS Enhanced Tag Based on Dielectric Resonator - Lens Combination," *Frequenz*, vol.74, no.1–2, pp. 1–8, 2020.

[8] S. Genovesi, F. Costa, F. Dicandia, M. Borgese and G. Manara, "Orientation-Insensitive and Normalization-Free Reading Chipless RFID System Based on Circular Polarization Interrogation," in *IEEE Transactions on Antennas and Propagation*, vol. 68, no. 3, pp. 2370–2378, March 2020.

[9] M. Khaliel, M. El-Hadidy and T. Kaiser, "Printable depolarizing chipless RFID tag based on DGS resonators for suppressing the clutter effects," *2015 9th European Conference on Antennas and Propagation (EuCAP)*, Lisbon, 2015, pp. 1–5.

[10] M. H. Hassan et al., "OAM Mode Order Conversion and Clutter Rejection With OAM-Coded RFID Tags," *IEEE Access*, vol. 8, pp. 218729–218738, 2020.

[11] V. Mulloni and M. Donelli. "Chipless RFID Sensors for the Internet of Things: Challenges and Opportunities," *Sensors*, vol. 20, no. 7, pp. , 2020.

[12] A. Lažaro et al., "Chipless Dielectric Constant Sensor for Structural Health Testing," *IEEE Sensors Journal*, vol. 18, no. 13, pp. 5576-5585, 2018.

[13] B. Kubina, M. Schüßler, C. Mandel, A. Mehmood, and R. Jakoby, "Wireless high-temperature sensing with a chipless tag based on a dielectric resonator antenna ", *IEEE SENSORS*, pp. 1–4, Nov. 2013.

[14] M. El-Absi, A. Alhaj Abbas, A. Abuelhaija, K. Solbach and T. Kaiser, "Chipless RFID Infrastructure Based Self-Localization: Testbed Evaluation," in *IEEE Veh. Tech.*, vol. 69, no. 7, pp. 7751–7761, July 2020.

[15] M. El-Absi, A. Alhaj Abbas, A. Abuelhaija, F. Zheng, K. Solbach and T. Kaiser, "High-accuracy indoor localization based on Chipless RFID systems at THz band," *IEEE Access*, vol. 6, pp. 54355–54368, 2018.

[16] N. Zhang, M. Hu, L. Shao, J. Yang, "Localization of Printed Chipless RFID in 3-D Space", *IEEE Microw. Wirel. Compon. Lett.*, 2016, 26, pp. 373–375.

[17] N. Karmakar, *Handbook of smart Antennas for RFID Systems.*, John Wiley & Sons, 2010.

[18] R. Miesen et al., "Where is the Tag?," *IEEE Microwave Magazine*, vol. 12, no. 7, pp. 49–63, Dec. 2011.

[19] J. Zhou, H. Zhang and L. Mo, "Two-dimension localization of passive RFID tags using AOA estimation," *2011 IEEE International Instrumentation and Measurement Technology Conference*, pp. 1–5, May 2011.

[20] A. Alhaj Abbas, M. El-Absi, A. Abuelhaija, K. Solbach and T. Kaiser, "Dielectric Resonator-Based Passive Chipless Tag with Angle-of-Arrival Sensing," *IEEE Transactions on Microwave Theory and Techniques*, vol. 67, no. 5, pp. 2010–2017, 2019.

[21] A. Vena, E. Perret and S. Tedjini, "A compact chipless RFID tag using polarization diversity for encoding and sensing," *2012 IEEE International Conference on RFID (RFID)*, Orlando, FL, USA, pp. 191-197, 2012.

[22] S. Genovesi, F. Costa, M. Borgese, F. A. Dicandia, A. Monorchio and G. Manara, "Chipless RFID sensor for rotation monitoring," *2017 IEEE International Conference on RFID Technology & Application (RFID-TA)*, Warsaw, pp. 233-236, 2017.

[23] S. Genovesi, F. Costa, M. Borgese, F. A. Dicandia, and G. Manara, "Chipless radio frequency identification (RFID) sensor for angular rotation monitoring," *Technologies*, vol. 6, no. 3, pp. 1–11, 2018.

[24] N. Barbot, O. Rance and E. Perret, "Angle Sensor Based on Chipless RFID Tag," *IEEE Antennas and Wireless Propagation Letters*, vol. 19, no. 2, pp. 233-237, Feb. 2020.

[25] N. Barbot, O. Rance and E. Perret, "Cross-Polarization Chipless Tag for Orientation Sensing," *2020 50th European Microwave Conference (EuMC)*, Utrecht, Netherlands, pp. 1119-1122, 2021.

[26] H. Song and T. Nagatsuma, "Present and Future of Terahertz Communications," *IEEE Transactions on Terahertz Science and Technology*, vol. 1, no. 1, pp. 256–263, Sept. 2011.

[27] A. Alhaj Abbas, M. El-Absi, A. Abuelhaijay, K. Solbach and T. Kaiser, "THz Passive RFID Tag Based on Dielectric Resonator Linear Array," *2019 Second International Workshop on Mobile Terahertz Systems (IWMTS)*, Bad Neuenahr, Germany, pp. 1-5, 2019.

[28] K. Solbach, A. Alhaj Abbas, M. El-Absi, A. Abuelhaija and T. Kaiser, "Experimental Demonstration of Double-Notch RCS Spectral Signature of Corner Reflector Tag for THz Self-Localization System," *2020 Third International Workshop on Mobile Terahertz Systems (IWMTS)*, Essen, Germany, pp. 1-4, 2020.

[29] M. Bernier, F. Garet, E. Perret, L. Duvillaret, and S. Tedjini, "Terahertz encoding approach for secured chipless radio frequency identification," *Appl. Opt.*, vol. 50, no. 23, pp. 4648–4655, 2011.

[30] Y. Kujime, M. Fujita, and T. Nagatsuma, "Terahertz Tag Using Photonic-Crystal Slabs," *J. Lightwave Technol.*, vol. 36, no. 19, pp. 4386–4392, 2018.

[31] A. Jimeňez-Sa'ez, M. M. Schüßler, D. Pandel, N. Benson and R. Jakoby, "3D Printed 90 GHz Frequency-Coded Chipless Wireless RFID Tag," *2019 IEEE MTT-S International Microwave Workshop Series on Advanced Materials and Processes for RF and THz Applications (IMWS-AMP)*, Bochum, Germany, pp. 4-6, 2019.

[32] A. Jimeňez-Saèz et al., "3D Printed Alumina for Low-Loss Millimeter Wave Components," *IEEE Access*, vol. 7, pp. 40719-40724, 2019.

[33] J. Joannopoulos, S. Johnson, J. Winn, and R. Meade, "Photonic Crystals: Molding the Flow of Light," 2nd edition, Princeton University Press, 2018.

[34] H. Macleod, "Thin-film optical filters," 3nd edition Institute of Physics Publishing, Bristol and Philadelphia, 2001.

[35] S. Dong-Mo, T. Zhi-Xiang, Z. Lei, S. Zhan, W. Shuang-Chun and F. Dian-Yuan, "Experimental demonstration of a low-pass spatial filter based on a one-dimensional photonic crystal with a defect layer," *Chinese Physics Letters*, vol. 30, no. 4, pp. 044206-1–044206-3, 2013.

[36] T. Griesser, C. Balanis, "Backscatter analysis of dihedral corner reflectors using physical optics and the physical theory of diffraction," *IEEE Transactions on Antennas and Propagation*, vol. 35, no. 10, pp. 1137–1147, 1987.

[37] A. Lazaro, J. Lorenzo, R. Villarino, D. Girbau, "Modulated corner reflector using frequency selective surfaces for FMCW radar applications," *Proceedings of 2015 European Microwave Conference (EuMC)*, pp. 111-114, 2015.

[38] A. Alhaj Abbas, M. El-Absi, A. Abuelhaija, K. Solbach, T. Kaiser, "Metallic reflectors with notched RCS spectral signature using dielectric Resonators," *Electronics Letters*, vol. 56, no. 6, pp. 273-276, 2020.

[39] A. Jimeňez-Saèz et al., "Frequency Selective Surface Coded Retroreflectors for Chipless Indoor Localization Tag Landmarks," *IEEE Antennas and Wireless Propagation Letters*, vol. 19, no. 5, pp. 726–730, May 2020.

[40] C. Wu, and Z. Wang, "Properties of defect modes in one-dimensional photonic crystals," *Progress In Electromagnetics Research*, vol. 103 , pp. 169-184, 2010.

[41] L. Maigyte, Lina, and K. Staliunas, "Spatial filtering with photonic crystals," *Applied physics reviews*, vol.2, no. 1, pp. 011102-1–011102-17, 2015.

[42] H. Němec, L. Duvillaret, F. Quemeneur , and P. Kužel, "Defect modes caused by twinning in one-dimensional photonic crystals" *JOSA B*, vol. 21, no. 3, pp. 548–553, 2014.

[43] R. Wang, J. Dong, and D. Xing, "Defect Studies in a One-Dimensional Photonic Band Gap Structure," *physica status solidi (b)*, vol. 200, pp.529-534, 1997.

[44] G. Panzarini et al., "Cavity-polariton dispersion and polarization splitting in single and coupled semiconductor microcavities," *Physics of the Solid State* vol. 41, no.8, pp. 1223-1238, 1999.

[45] V. Savona, L. Andreani, P. Schwendimann, and A. Quattropani, "Quantum well excitons in semiconductor microcavities: Unified treatment of weak and strong coupling regimes" *Solid State Communications*, vol. 93, no. 9, pp. 733-739, 1995.

[46] D. Babic and S. Corzine, "Analytic expressions for the reflection delay, penetration depth, and absorptance of quarter-wave dielectric mirrors," *IEEE Journal of Quantum Electronics*, vol. 28, no. 2, pp. 514-524, Feb. 1992.

[47] M. Born and E. Wolf, "Principles of Optics," 6nd edition, Oxford; New York: Pergamon Press, 1980.

[48] M. Khaliel, A. El-Awamry, A. Fawky Megahed and T. Kaiser, "A Novel Design Approach for Co/Cross-Polarizing Chipless RFID Tags of High Coding Capacity," *IEEE Journal of Radio Frequency Identification*, vol. 1, no. 2, pp. 135-143, June 2017.

[49] H. Hirosawa and Y. Matsuzaka, "Calibration of a cross-polarized SAR image using dihedral corner reflectors," *IEEE Transactions on Geoscience and Remote Sensing*, vol. 26, no. 5, pp. 697–700, Sept. 1988.

[50] Rogers Corporation. RT/Duroid 6006 and 6010 LM Laminate Data Sheet. Accessed: [Online]. Available: https://www.rogerscorp.com/-/media/project/rogerscorp/documents/advanced-connectivity-solutions/english/data-sheets/rt-duroid-6006-6010lm-laminate-data-sheet.pdf.

[51] M. Polivka, J. Havlicek, M. Svanda and J. Machac, "Improvement in Robustness and Recognizability of RCS Response of U-Shaped Strip-Based Chipless RFID Tags," *IEEE Antennas and Wireless Propagation Letters*, vol. 15, pp. 2000-2003, 2016.

[52] A. Vena, E. Perret and S. Tedjni, "A Depolarizing Chipless RFID Tag for Robust Detection and Its FCC Compliant UWB Reading System," *IEEE Transactions on Microwave Theory and Techniques*, vol. 61, no. 8, pp. 2982-2994, Aug. 2013.

[53] F. Eugene and M. Tulley, “Radar Cross Section”. Rijeka, Croatia: SciTech, 2004.

[54] J. Barowski et al., “Design and Evaluation of a Passive Frequency-Coded Reflector using W-Band FMCW Radar,” *2020 German Microwave Conference (GeMiC)*, Cottbus, Germany, 2020, pp. 92-95.

[55] C. Mandel et al., “Approach for long-range frequency domain chipless RFID tags towards THz,” *Smart SysTech 2016; European Conference on Smart Objects, Systems and Technologies*, Duisburg, Germany, 2016, pp. 1–7.

[56] A. El-Awamry, A. Fawky, M. El-Hadidy and T. Kaiser, “smart notch detection techniques for robust frequency coded chipless RFID systems,” *2015 9th European Conference on Antennas and Propagation (EuCAP)*, Lisbon, Portugal, 2015, pp. 1–5.

[57] A. Fawky, A. El-Awamry, M. Khaliel and T. Kaiser, “Novel notch detection techniques for Frequency Coded chipless RFID,” *2017 IEEE 14th International Conference on Networking, Sensing and Control (ICNSC)*, Calabria, Italy, 2017, pp. 345–350.